Predicting DNA damage response in non-small cell lung cancer organoids via simultaneous label-free autofluorescence multiharmonic microscopy

Terrence T. Roh [a,b], Aneesh Alex [a,b], Prasanna M. Chandramouleeswaran [b], Janet E. Sorrells [a,e], Alexander Ho [a,e], Rishyashring R. Iyer [a,d], Darold R. Spillman Jr. [a,g], Marina Marjanovic [a,e,g], Jason E. Ekert [b], BanuPriya Sridharan [b], Balabhaskar Prabhakarpandian [b], Steve R. Hood [a,c], Stephen A. Boppart [a,d,e,f,g,*]

[a] GSK Center for Optical Molecular Imaging, Beckman Institute for Advanced Science and Technology, University of Illinois Urbana-Champaign, Urbana, IL, 61801, USA
[b] In Vitro In Vivo Translation, GSK plc, Collegeville, PA, 19426, USA
[c] In Vitro In Vivo Translation, GSK plc, Stevenage, SG1 2NY, UK
[d] Department of Electrical and Computer Engineering, University of Illinois Urbana-Champaign, Urbana, IL, 61801, USA
[e] Department of Bioengineering, University of Illinois Urbana-Champaign, Urbana, IL, 61801, USA
[f] Cancer Center at Illinois, University of Illinois Urbana-Champaign, Urbana, IL, 61801, USA
[g] NIH/NIBIB Center for Label-free Imaging and Multi-scale Biophotonics (CLIMB), University of Illinois Urbana-Champaign, Urbana, IL, 61801, USA

ARTICLE INFO

ABSTRACT

The DNA damage response (DDR) is a fundamental readout for evaluating efficacy of cancer therapeutics, many of which target DNA associated processes. Current techniques to evaluate DDR rely on immunostaining for phosphorylated histone H2AX (γH2AX), which is an indicator of DNA double-strand breaks. While γH2AX immunostaining can provide a snapshot of DDR in fixed cell and tissue samples, this method is technically cumbersome due to temporal monitoring of DDR requiring timepoint replicates, extensive assay development efforts for 3D cell culture samples such as organoids, and time-consuming protocols for γH2AX immunostaining and its evaluation. The goal of this current study is to reduce overall burden on assay duration and development in non-small cell lung cancer (NSCLC) organoids by leveraging label-free multiphoton imaging. In this study, simultaneous label-free autofluorescence multiharmonic (SLAM) microscopy was used to provide rich intracellular information based on endogenous contrasts. SLAM microscopy enables imaging of live samples eliminating the need to generate sacrificial sample replicates and has improved image acquisition in 3D space over conventional confocal microscopy. Predictive modeling between label-free SLAM microscopy and γH2AX immunostained images confirmed strong correlation between SLAM image features and γH2AX signal. Across multiple DNA targeting chemotherapeutics and multiple patient-derived NSCLC organoid lines, the optical redox ratio and third harmonic generation channels were used to robustly predict DDR. Imaging via SLAM microscopy can be used to more rapidly predict DDR in live 3D NSCLC organoids with minimal sample handling and without labeling.

1. Introduction

Cancer treatments can selectively target tumor tissues by inhibiting synthetically lethal pathways for DNA repair [1,2]. *In vitro* screening for synthetically lethal drugs exploits the formation of phosphorylated histone H2AX (γH2AX) at sites of DNA double-strand breaks (DSBs) to evaluate DNA damage response (DDR) induced by drug candidates.

γH2AX formation precedes localization of repair proteins to sites of DSBs and can be labeled via immunostaining [3]. While this labeling approach is suitable for screening programs using 2D cultured cells, γH2AX labeling and analysis in 3D organoids requires significant assay optimizations such as removing Matrigel content and chemical clearing [4,5]. Moreover, the need for sacrificial fixation and immunostaining adds significant time and resource challenges when performing

longitudinal assays, especially in complex *in vitro* models such as organoids.

Recently, advances in label-free, multiphoton microscopy have enabled endpoint predictions such as apoptosis via fluorescence lifetime imaging [6] and DNA damage using Raman micro-spectroscopy [7]. These multiphoton microscopy techniques rely on endogenous molecular signals, avoiding the need to process the sample and have improved signal acquisition through thicker samples than for single photon microscopy techniques such as confocal microscopy [8]. Studies using label-free microscopy often leverage the unique fluorescence profiles of endogenous flavin adenine dinucleotide (FAD) and reduced nicotinamide adenine dinucleotide phosphate/nicotinamide adenine dinucleotide (NAD(P)H) to assess cell metabolism [9–11]. FAD and NAD(P)H are metabolic enzymes that enable ATP generation by shuttling electrons through the electron transport chain via oxidation of NAD(P)H to NAD(P)+ and $FADH_2$ to FAD. Since only NAD(P)H and FAD endogenously emit fluorescence, the ratio between FAD and NAD(P)H fluorescence can be used to inform the cell redox state, also known as the optical redox ratio (RR). Changes in the RR indicate shifts between glucose catabolism and oxidative phosphorylation and is linked to DDR through metabolism of NAD(P)+ via enzymatic action of poly-ADP ribose polymerase (PARP) which also reduces levels of NAD(P)H [12–15]. Measurements of the RR have been used to track cell differentiation [16], therapeutic response to cancer treatment [17], and inform metastatic potential of cancer cells [11]. While prior studies have shown that DDR results in altered redox homeostasis [12–14], no studies to our knowledge have used label-free optical readouts such as RR to predict DDR.

In this study, a label-free prediction model is developed for patient derived tumor organoids which are 3D *in vitro* cellular platforms that retain the molecular signatures of the original donor while preserving patient specific drug resistances [18–21]. Recent approaches towards predicting biological outcomes of organoids have utilized cell paint which uses fluorescently labeled organelles to generate a phenotypic profile for predictions [5,22]. However, this approach can be resource intensive in complex *in vitro* models due to the need to generate sample sets for each timepoint. In this study, a label-free phenotypic approach via SLAM microscopy is devised for prediction of DDR by live imaging of treatment naïve non-small cell lung cancer (NSCLC) organoids.

The prediction was trained using extracted label-free SLAM features and γH2AX quantifications from 2D organoids. The use of 2D organoids was central to model training because 2D organoids remain spatially fixed during the immunofluorescent labeling process enabling label-free SLAM imaging across a field-of-view (FOV) followed by γH2AX labeled immunofluorescence imaging on the same FOV. This produces label-free and labeled image pairs with accurate spatial representations and co-registration which can be used train a prediction model to understand how label-free SLAM microscopy features indicate DDR through -H2AX expression in 3D organoids. The implementation of a prediction model trained on 2D organoids and then implemented on 3D organoids was facilitated by the optical sectioning and improved z-depth penetration inherent in multiphoton microscopy techniques such as SLAM microscopy.

Previous studies using SLAM microscopy have been used to identify optical signatures of breast cancer tissue in histological sections [23], quantify tumor microenvironment cellular and extracellular vesicle compositions [24], and 3D real-time histology of unprocessed human and rat tissue [25]. Here, SLAM microscopy was used to capture the metabolic signatures of organoids via 2-photon autofluorescence (2PF) of FAD and 3-photon autofluorescence (3PF) of NAD(P)H, and third harmonic generation (THG) for structural features [26–28]. Second harmonic generation (SHG) was also captured but since organoids have limited birefringence or collagen, little to no SHG signal was present. SLAM microscopy uses a near-infrared laser source, improving light penetration through thick samples and decreasing thermally induced photodamage to the sample by relying on multiphoton interactions at focal volumes. SLAM microscopy relies on autofluorescence which Matrigel proteins do not emit enabling organoids in Matrigel to be imaged without additional processing, better preserving the microstructure and the imaging properties between 2D and 3D organoid platforms and enabling implementation of SLAM-based prediction models derived from data on 2D organoids to be applied to 3D organoids.

2. Materials and methods

2.1. Organoid culture

Treatment naïve NSCLC organoids which were derived from three independent donors (HUB-07-B2-047, HUB-07-B2-065, and HUB-07-B2-133 referred to as HUB047, HUB065, HUB133 respectively), were originally obtained from Hubrecht Organoid Technology (Utrecht, Netherlands). The human biological samples were sourced ethically and their research use was in accord with the terms of the informed consents under an IRB/EC approved protocol. After thawing from a cryovial, 500 μL of organoid suspensions were centrifuged at 4 °C at 1500 rpm and resuspended in 100 μL of 80 % growth factor-reduced Matrigel (Corning, 356231) and plated on 24-wellplates (Greiner, 662160) at three 10 μL droplets per well. The droplets were gelled at 37 °C in a cell culture incubator for 30 min and 500 μL of culture media was added. The culture media was refreshed every other day and consisted of Advanced Dulbecco's Modified Eagles Medium with Nutrient Mixture F-12 Hams (ThermoFisher, 12634028), 2 mM GlutaMax (ThermoFisher, 35050038), 10 mM HEPES (ThermoFisher, 35050038), 1.25 mM N-Acetyl cysteine (Sigma Aldrich, A9165-25G), 500 nM A83-01 (Tocris, 2939-10 mg), 1x B27 supplement (ThermoFisher, 17504044), 25 ng/mL FGF7 (Peprotech, 100-19), 100 ng/mL FGF10 (Peprotech, 100-26), 50 ng/mL Noggin (Peprotech, 120-10C), 5 mM Nicotinamide (Sigma Aldrich, N0636-100G), 50 μg/mL Primocin (InvivoGen, ANT-PM-2), 250 ng/mL Rspondin-3 (R&D Systems, Bulk 3500-RS/CF), 500 nM SB202190 (Sigma Aldrich, S7076-25 mg), and 5 μM Y-27632 (Sigma Aldrich, NC1632222). At confluency, organoids were passaged according to protocols based on the work by Pleguezuelos-Manzano et al. [29]. Organoids used in this study were at passage 2 after thawing from cryovials.

Two-dimensional organoids were cultured from 3D NSCLC organoids derived from treatment naïve patients using protocols used to generate 2D organoids of epithelial tissue [30]. Briefly, 3D organoids cultured in wellplates were collected with surrounding media in 0.5 mM EDTA in PBS (ThermoFisher, AM9260G) and centrifuged at 1500 rpm at 8 °C for 5 min. The supernatant was removed, and the pellet was digested in 1 mL of 0.05 % Trypsin-EDTA (Thermofisher, 25-300-054) for 4 min. The trypsin was inactivated by adding 1 mL of culture media and the organoid suspension was mechanically disrupted by pipetting 50 times through a P1000 tip. The organoid suspension was then passed through a 40 μm strainer (Falcon, 352340) and then centrifuged again at 1500 rpm at 8 °C for 5 min. After removing the supernatant, the pellet containing organoid-derived single cells was resuspended in complete culture media. A 40 μL volume of the organoid suspension at 2-3 $\times$ 10^5 cells/mL was plated in each well of a 384 wellplate (PerkinElmer, 6057308) to establish 2D organoids.

2.2. Compound addition

Etoposide (CAS ID: 33419-42-0), bortezomib (CAS ID: 179324-69-7), olaparib (CAS ID: 763113-22-0), and cisplatin (CAS ID: 15663-27-1) were initially diluted to 10 mM DMSO (dimethyl sulfoxide) stocks and frozen. Compounds were thawed and added to phenol-free complete media to final concentrations prior to experiment start. Total volume of DMSO added to organoid complete media during this step and with vehicle control remained constant between experiments. 2D and 3D organoids were treated by replacing the complete culture media with the

compound-laden culture media. The media with treatment was replaced prior to label-free imaging, occurring every two or three days, resulting in a continuous treatment regimen.

2.3. SLAM microscopy

The SLAM microscopy technique was first developed and demonstrated by You et al. [26]. The optical imaging hardware used in this study for SLAM microscopy was previously described by Lee et al. [31]. Briefly, a high peak power femtosecond laser centered at 1040 nm (Spectra-Physics, Femtotrain) was operated at a 10 MHz pulse repetition rate. The laser beam was used to pump a nonlinear photonic crystal fiber (NKT Photonics, LMA-PM-15) to generate a supercontinuum which was then sent to a pulse shaper (Biophotonics Solutions Inc., FemtoJock-D) to tailor the pulses to a bandwidth from 980 nm to 1100 nm. The beam was delivered to a 25x, 1.05 NA water-immersion objective lens (Olympus, XLPLN25XWMP2) with an average power of 10 mW at the sample plane. Four sequential sets of dichroic beam splitters and bandpass filters (Semrock) were used to separate the collected signal (334–404 nm for THG, 405–504 nm for 3PF, 542–566 nm for SHG, 593–700 nm for 2PF). A 2D piezoelectric stage (SmarAct, SLC-24150-LC) was used to collect images from the sample. The FOV was set to 180 μm × 180 μm. Samples were cultured in phenol-free media for the duration of the experiment to avoid signal interference from phenol autofluorescence, and imaged while enclosed in a stage-top incubator (TOKAI HIT Co., STXF-WSKMX-SET).

In addition to the benchtop SLAM microscope, a portable SLAM imaging system (LiveBx LLC, Model: FreeView) was used to capture images of organoids monolayers for dose response experiments in this study. The laser source in this system was a femtosecond laser (Satsuma, Amplitude) centered at 1030 nm with a pulse duration of 300 fs and a pulse repetition rate of 5 MHz. The laser pulses were passed through a photonic crystal fiber (NKT Photonics, LMA-25) to generate the super-continuum needed for SLAM microscopy. A motorized half-wave plate was used to adjust the output power level at the sample, and a pulse compressor (Swamp Optics LLC, BOA-1050) was used to compensate for the dispersion introduced by the system optics and to compress the pulses down to 40 fs for efficient multiphoton excitation. The output light from the pulse compressor was directed towards a silicone immersion 30x, 1.05 NA objective lens (Olympus, UPANSAPO30XS). The laser beam was raster scanned on the sample using a galvanometric scanning mirror pair. The signal emitted from the sample was collected through the same objective lens in the epi-direction and was spectrally separated using dichroic beam splitters and bandpass filters corresponding to various SLAM detection channels (335–355 nm for THG, 417–477 nm for 3PF, 498–520 nm for SHG and 593–643 nm for 2PF). The FOV was set to 200 μm × 200 μm and images were taken with an average power at 2 mW at the sample plane while enclosed in the stage-top incubator.

For 2D organoids, each biological replicate was imaged at 3 different locations, across 3 biological replicates per timepoint and treatment group. Each sample was imaged first with SLAM and then with confocal microscopy after immunofluorescence staining for γH2AX foci. For 3D organoids, 3 individual organoids were imaged at 3 equidistant z-depths (10–20 μm spacing) per biological replicate with 4 biological replicates per treatment group per timepoint (Sfig. 3).

2.4. γH2AX foci immunostaining and imaging of 2D organoids

Two-dimensional (2D) organoid samples were fixed in 4 % para-formaldehyde (AAJ19943K2, ThermoFisher) for 30 min before rinsing in PBS 3 times and permeabilization in 0.25 % Triton X-100 (Sigma-Aldrich, AAA16046AE) for 15 min at room temperature. Samples were rinsed in PBS once, then incubated in a 3 % BSA solution (Sigma-Aldrich, A6003) for 1 h, prior to incubation with a solution of 1:500 phospho-histone H2A.X (Ser139) primary antibody (Invitrogen, MA5-27753)

overnight in 4 °C. Samples were then rinsed with PBS 3 times. A secondary antibody solution consisting of 1:500 Alexa 488 (ThermoFisher, A11001) and 1:1000 DAPI (ThermoFisher, EN62248) in 3 % BSA was applied for 1 h at room temperature prior to 3 more PBS rinses. The 2D organoid samples were then imaged using a Zeiss LSM 700 Confocal at Nyquist settings. Each FOV from the 2D organoids was identified by location and morphology annotations from the corresponding FOV from the label-free SLAM images. γH2AX quantification from these images was performed in CellProfiler [32].

2.5. γH2AX foci immunostaining and imaging for 3D organoids

To enable γH2AX imaging in 3D organoids cultured in 80 % Matrigel, organoids were extracted from the Matrigel at each timepoint. Organoid cultures from each treatment and timepoint group were collected and gently dissociated by pipetting in a 10 mL pipette prior to centrifugation at 1500 rpm for 5 min at 8 °C. The supernatant was then aspirated and 2 mL of dispase (Gibco, 17105041) was added. After incubation for 30 min, the resultant suspension was centrifuged at the previous settings. The supernatant was again removed, and the pellet was resuspended in Advanced Dulbecco's Modified Eagles Medium with Nutrient Mixture F-12 Hams, 2 mM GlutaMax, and 10 mM HEPES at 10,000 organoids per mL. A 40 μL volume of this solution was added to each of 3 wells in a 384 wellplate (PerkinElmer, 6057308) per group.

Wellplates containing organoid suspensions were centrifuged at 200 rpm for 5 s prior to each aspiration step to ensure that the organoids remained at the wellplate bottom. A 40 μL volume of 4 % para-formaldehyde (Sigma-Aldrich, HT5011-15 ML) was added to each well for 1 h at 4 °C. The paraformaldehyde solution was then replaced and rinsed with 40 μL of 0.1 % Tween 20 (Sigma-Alrich, P1379) in PBS 3 times before incubation overnight at 4 °C. The samples were then rinsed twice in washing buffer consisting of PBS and 0.2 wt% BSA (Sigma-Aldrich, A9647) and 0.1 % Triton X-100 (Sigma-Aldrich, T8787-100 ML). Afterwards, samples were incubated overnight at 4 °C on a shaker plate at 150 rpm in washing buffer containing 1:500 of phospho-histone H2A.X (Ser139) primary antibody. The primary antibody solution was then replaced with a secondary antibody solution consisting of 1:500 Alexa 647 (ThermoFisher, A32728) and 1:500 DAPI in PBS. Samples were incubated overnight at 4 °C on a shaker plate at 150 rpm and then washed 3 times with 40 μL of washing buffer. Samples were chemically cleared sequentially in 50 % meOH, 80 % meOH and 100 % meOH (Merck, 34860-100 ML-R). A 40 μL volume of clearing agent (Invitrogen, V11325) was added to each well for 15 min at room temperature prior to imaging. Each well was completely imaged at 20× using a PerkinElmer OperaPhenix (1400L17141). Maximum projections of z-stacks obtained at 20 μm spacing were quantified for γH2AX using CellProfiler.

2.6. Data analysis

Optical RR images were generated as shown in Fig. 2B [27]. SLAM intensity, texture, and rank-weighted-correlation features were extracted using Python 3.10 on segmented SLAM images (scikit-image, mahotas). Segmentation masks were obtained using Ilastik on 3PF images [33]. Min-max scaling was applied on extracted features and correlated to γH2AX foci/nuclei quantification in 2D organoids using a gradient boost regressor model using the Python package sci-kit learn. Feature selection was done by ranking the features based on feature importance through an initial gradient boost regressor and selecting the top 27 SLAM features. Feature selection was done to improve model performance by removing superfluous features. The gradient boost regressor model was trained on top features for validation on SLAM features from 3D organoids. Validation consisted of a train/test split of 80 %/20 % with the 2D organoid dataset and on a new dataset generated from 3D organoids treated with DNA damaging compounds not included in the training data.

One-way ANOVA testing followed by the Tukey's Post hoc test was

applied on data with equal variances and normal distributions. Otherwise, a Kruskal-Wallis H-test was performed followed with Dunn's multiple comparison test.

3. Results

3.1. SLAM microscopy for live cell imaging

SLAM microscopy uses non-linear interactions between light and sample, confining absorption and fluorescence within a focal volume and limiting photodamage and photobleaching [34]. In contrast to confocal microscopy, SLAM microscopy uses a lower energy, near-infrared excitation laser with shorter pulse durations to further reduce the photodamage in biological samples (Fig. 1a). Short pixel dwell times (<10 μs) with multi-frame averaging was used to further reduce photodamage at the focal volume. Prior studies using this approach show no apparent signs of photodamage in live cell samples [35,36]. SLAM imaging channels (THG, 2PF, 3PF) are specific for the endogenous fluorescence produced by optical heterogeneity (THG), FAD (2PF), and NAD(P)H (3PF) (Fig. 1b). Noninvasive SLAM imaging of organoids in either 2D and 3D formats enables acquisition of molecular/metabolic signal from autofluorescence with high-resolution optical sectioning (Fig. 1c), providing rich metabolic and structural information from defined z-slices.

3.2. Label-free imaging of DNA damage response (DDR) to chemotherapeutic treatments

Under brightfield microscopy, NSCLC organoids in Matrigel culture

present as multicellular structures with cystic or compact morphology (Fig. 2a). Similarly, SLAM microscopy can visualize organoid morphology, however SLAM microscopy images a 2D optical slice of the 3D structure, highlighting the hollow morphology of these organoids (Fig. 2b). Moreover, SLAM microscopy provides functional information in the form of the optical RR which provides metabolic information and can be calculated from the intensities in the 2 PF and 3 PF channels which correspond to signal from FAD and NAD(P)H fluorescence respectively (Fig. 2b). The optical RR is a measure of the oxidation-reduction balance and a robust indicator of metabolic state which can be used in conjunction with the THG channel to obtain a label-free phenotypic profile of organoid cultures [10,37,38]. Using label-free SLAM images, DDR was extrapolated by implementing a prediction model which was trained using a gradient boost regression model on a dataset comprised of SLAM phenotypic profiles linked to the ground truth of γH2AX foci/nuclei counts (Fig. 2c).

3.3. Training images generated with label-free SLAM imaging and label-based γH2AX immunostaining

To generate a training dataset for a DDR regression model, 2D organoid samples derived from HUB-047 organoids were first imaged using SLAM microscopy, followed by γH2AX foci immunofluorescence imaging for ground truth (Fig. 3a). To discriminate cell death mediated through non-DDR pathways from DDR, the training data included organoids treated with bortezomib, a proteasome inhibitor which induces cell death without DDR [39] (Fig. 3a). DDR was induced using etoposide, a topoisomerase inhibitor which results in DNA damage [40]. A total of 144 SLAM FOVs, split across media control, DMSO Vehicle, 3
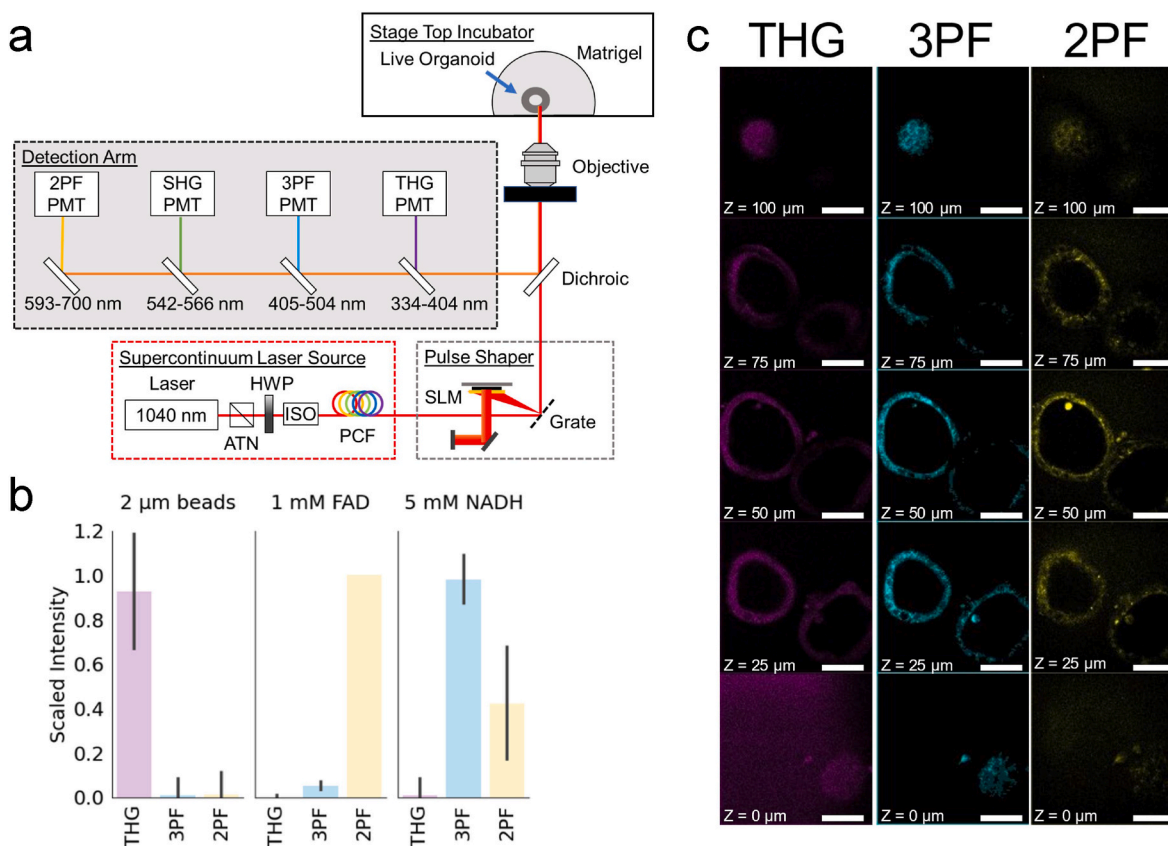

Fig. 1. Simultaneous Label-free Autofluorescence Multiharmonic (SLAM) microscopy visualizes label-free signals. a) SLAM microscopy uses a modified ultrafast laser to excite and detect 4 orthogonal endogenous signals. b) THG, 3PF, and 2PF endogenous signals corresponding to sample heterogeneity via THG signal, reduced nicotinamide adenine dinucleotide/reduced nicotinamide adenine dinucleotide (NAD(P)H) signal via 3PF, and flavin adenine dinucleotide (FAD) via 2PF. Signal intensities were collected from 1 field of view of each sample. c) Optically sectioned THG, 3PF, and 2PF signal is generated in organoids across multiple depths denoted by z.

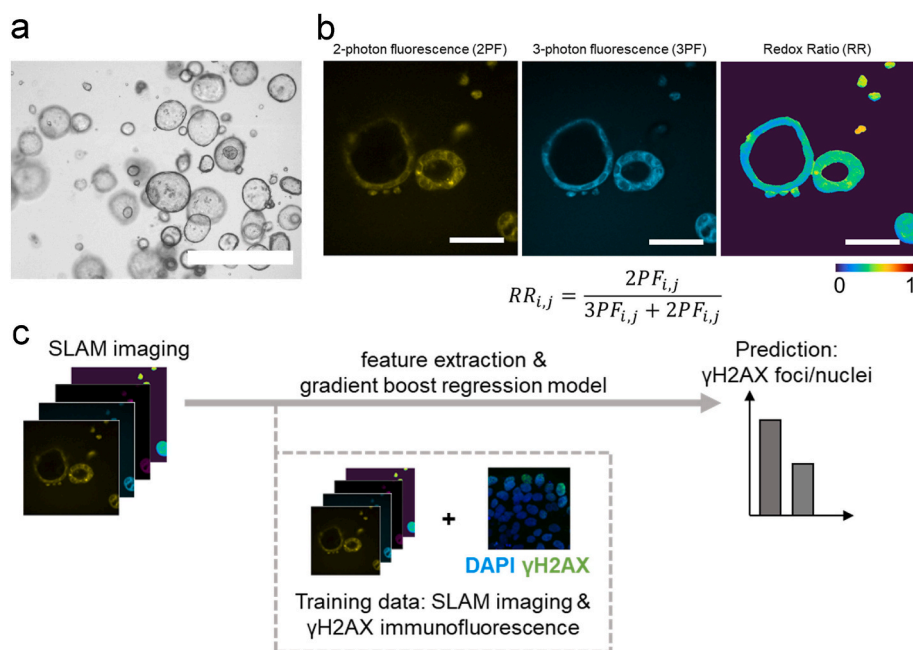$$RR_{i,j} = \frac{2PF_{i,j}}{3PF_{i,j} + 2PF_{i,j}}$$

Fig. 2. SLAM microscopy enables simultaneous visualization of FAD, NAD(P)H, and THG signals to inform prediction of DNA damage response in live samples. a) Brightfield image of NSCLC organoids shows multicellular 3D structures (scalebar: 1000 μm). b) Optical redox ratio (RR) images were generated from ratio of 2 PF FAD signal and 3 PF NAD(P)H signal (scalebars: 50 μm). c) A prediction model for DNA damage response was created by training a gradient boost regression model on linked feature sets of label-free SLAM images and labeled γH2AX foci-stained immunofluorescence images as ground truth.

μM etoposide, 30 μM etoposide, and 10 μM bortezomib treatment groups were paired with their corresponding ground truth γH2AX foci/nuclei values. In all FOVs capturing the growing edges of cell growth, γH2AX foci signal was observed to be higher which we hypothesize is due to replicative stress [41]. FOVs from media control and DMSO vehicle displayed a baseline γH2AX signal which was expected since a baseline amount of DSBs are formed per cell cycle in normal human cells [42] (Fig. 3d).

Features extracted from THG, 2PF, 3PF and RR images include intensity-based features, Haralick texture features [43], and rank-weighted co-localization [44]. The AUC-RR value was included as a handcrafted optical RR derived intensity feature, constructed based on two assumptions about the relationship between optical RR and cell metabolism (Sfig. 2). Firstly, the relationship between metabolism and optical RR is assumed to be a linear relationship between the optical RR and the rate of change of the metabolism. This differs from the conventional assumption that optical RR values correlate directly with metabolic status of samples but aligns with our experimental observation that optical RR intensities are highest at early timepoints where the greatest γH2AX foci/nuclei change occur (Fig. 3c and d). The second assumption is that optical RR intensity can be separated into a $RR_{control}$ representing the metabolism at baseline and an RR_{effect} which captures the perturbation to metabolism caused by treatment. The AUC-RR feature is derived from the RR_{effect} which normalizes this value against a baseline metabolism that may differ between cell sources. Based on these assumptions, the AUC-RR feature can quantify cumulative metabolic change in live cell samples (Sfig 2, Fig 3b).

3.4. Metabolic and intracellular structural imaging features inform DNA damage response (DDR) prediction

Feature ranking was performed using an initial gradient boost regression and the top 27 ranked features were used to train the final DDR prediction model (Fig. 4c). Feature importance scores from the final model indicated that AUC-RR best informed the DDR prediction (Fig. 4c). Following the AUC-RR feature, the prediction model also relied on structural THG imaging features, HXY1 and HXY2.

Interestingly, THG texture and correlation features were more informative towards prediction than THG intensity features, suggesting that the spatial patterns of THG signal were important for DDR prediction and suggesting significant intracellular rearrangement of organelles (Fig. 4c). Evaluation of prediction and actual values based on 80 % train and 20 % test splits showed an R^2 score of 0.60 with a mean squared error of 3.2 γH2AX foci/nuclei, suggesting good performance of this model to predict DDR based on label-free SLAM imaging features (Fig. 4a and b). Removing the top feature, AUC-RR, resulted in an R^2 score of 0.29 with prediction of etoposide treated groups suffering the most, suggesting that the optical RR alone may not adequately predict metabolically involved cell events (Sfig. 3).

To further examine the relationship between the top feature, AUC-RR, and γH2AX foci/nuclei, a dose response for etoposide and bortezomib study was performed in HUB-047 organoid monolayers (Fig. 4d and e). In these experiments, a different SLAM system was used but reproduced the relationship between AUC-RR values and γH2AX foci/nuclei throughout this study. AUC-RR resulted in wider variation at all doses compared to γH2AX foci/nuclei which reflects the sampling used in SLAM imaging (~1 % of well area) as opposed to γH2AX foci immunofluorescence (100 % of well area). Fig. 4d shows that both AUC-RR and γH2AX foci/nuclei show similar dose response relationships to etoposide treatment. Similarly, in Fig. 4e, both AUC-RR quantification and γH2AX foci/nuclei show a steep decrease after 0.01 μM bortezomib treatment. In Fig. 4d and e, the original signed AUC-RR values are shown which better mirror positive and negative trends in γH2AX foci response across dosages of etoposide and bortezomib.

3.5. DNA damage prediction in 3D organoid samples

To validate SLAM based DDR prediction in organoids, the prediction model was implemented on 3D NSCLC (HUB047) organoids treated with etoposide, bortezomib, and two new DNA damaging compounds, cisplatin and olaparib. SLAM microscopy of 3D organoids embedded in Matrigel leverages optical sectioning at defined z-depths, generating 2D image slices of the 3D structure (Figs. 1c and 5a). A prediction-based DDR approach with SLAM microscopy enabled collection of
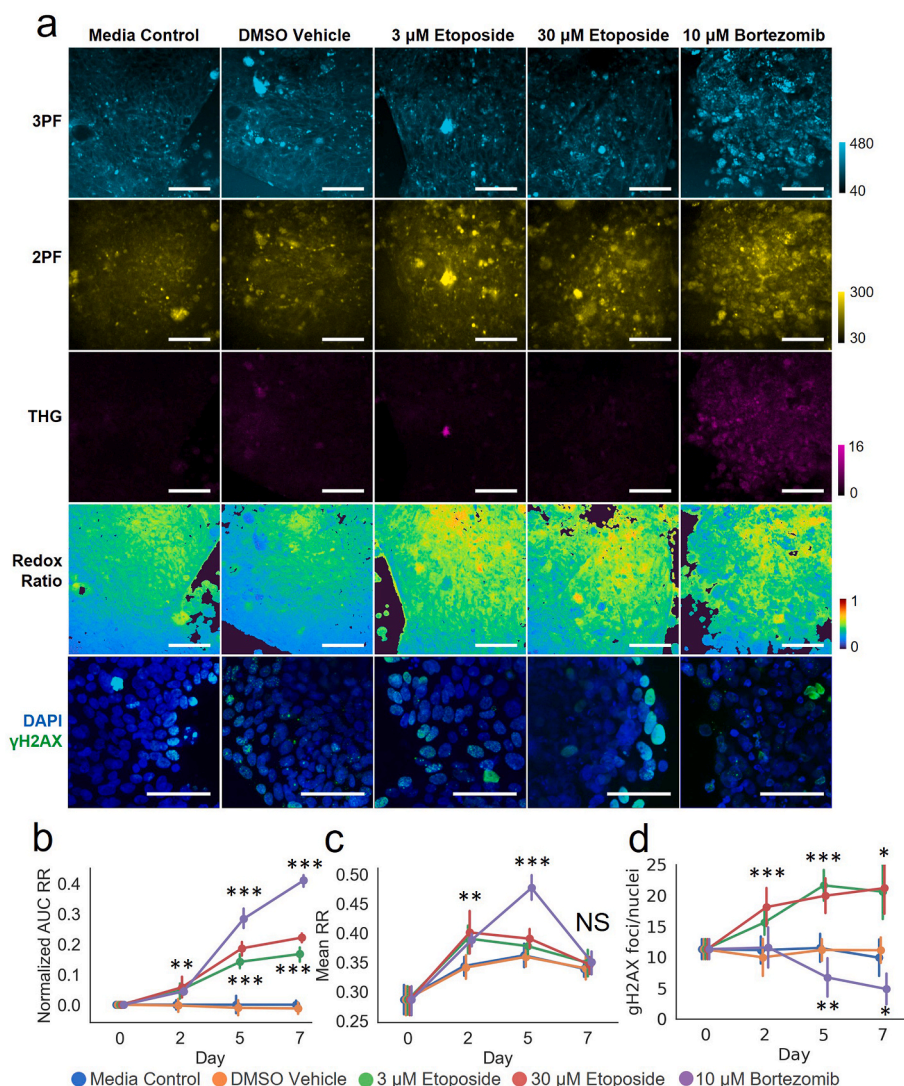
Fig. 3. Extracted features and readouts for model training and evaluation. 2D organoid monolayers from a treatment naïve patient were continuously treated with etoposide or bortezomib to generate a training dataset. a) Representative images taken at Day 2 of the NSCLC organoid monolayer using SLAM (3PF, 2PF, THG, RR) and immunofluorescence (DAPI, γH2AX). b) Area under the curve of the redox ratio (AUC RR) is increased relative to blank controls, demonstrating treatment effects on metabolism. c) Mean redox ratio shows a gradual increase then decrease in treatment groups. d) γH2AX foci/nuclei quantification. b,c,d) Statistical testing was performed using ANOVA followed by Tukey's post-hoc test or Kruskal-Wallis followed by Dunn's post-hoc test across all groups within each timepoint. Significance from media control indicated. No statistical differences were detected between media control and DMSO vehicle treatments across all timepoints (3 biological replicates with 3 technical replicates per biological replicate, NS = no significance, *$p < 0.05$, **$p < 0.01$, ***$p < 0.001$).

longitudinal DDR data from the same samples, whereas γH2AX foci labeling required sacrificial samples for each timepoint (Sfig. 4a and b). Implementation of the trained prediction model on SLAM images acquired from 3D organoids show that etoposide and cisplatin induce DDR but not olaparib (Fig. 5d). A separate parallel experiment where γH2AX foci labeling and quantification was performed similarly show increased DDR with etoposide and cisplatin but not olaparib in this NSCLC organoid line (Fig. 5b and c). Olaparib, a PARP inhibitor known for synthetic lethal interactions in BRCA-mutated tumors, showed no significant effects, which was supported by the lack of BRCA mutations in this organoid line. The DDR prediction model also correctly identified bortezomib treatment resulting in decreased DDR at days 2 and 5 (Fig. 5c and d). In agreement with previous observations (Figs. 3b and 4d), increases in the AUC-RR feature tracked closely with the treatment effect from DNA damaging agents (Fig. 5e). The performance of this model in this validation study supports its translation from 2D to 3D organoid formats and across DNA damaging treatments in HUB047 organoids.

3.6. AUC-RR feature is unchanged in etoposide resistant organoids

In this study, the AUC-RR feature was found to correlate with the extent of DDR (Figs. 3b, 4d and 5b, e). To test if the AUC-RR feature could be used to test sensitivity to DNA damaging treatments, three different NSCLC organoid lines were dosed with 3 μM etoposide and the AUC-RR quantifications were compared against DMSO vehicle. Representative optical RR images at Day 3 show regions of increased optical RR in only the HUB-047 line treated with etoposide at Day 3 (Fig. 6a). HUB065 and HUB133 showed no observable differences in RR between DMSO vehicle and etoposide treatment (Fig. 6b and c). Quantification of AUC-RR in each of the three lines (Fig. 6d) demonstrated similar trends with only HUB047 showing a significant increase. This was validated in a separate ground truth experiment with γH2AX foci/nuclei quantification, showing an increase in only the HUB047 organoids (Fig. 6e and Sfig. 6). AUC-RR had no statistically significant differences in HUB065 and HUB133, mirroring the γH2AX foci/nuclei quantification. In addition to label-free DDR prediction, SLAM microscopy may also be used to
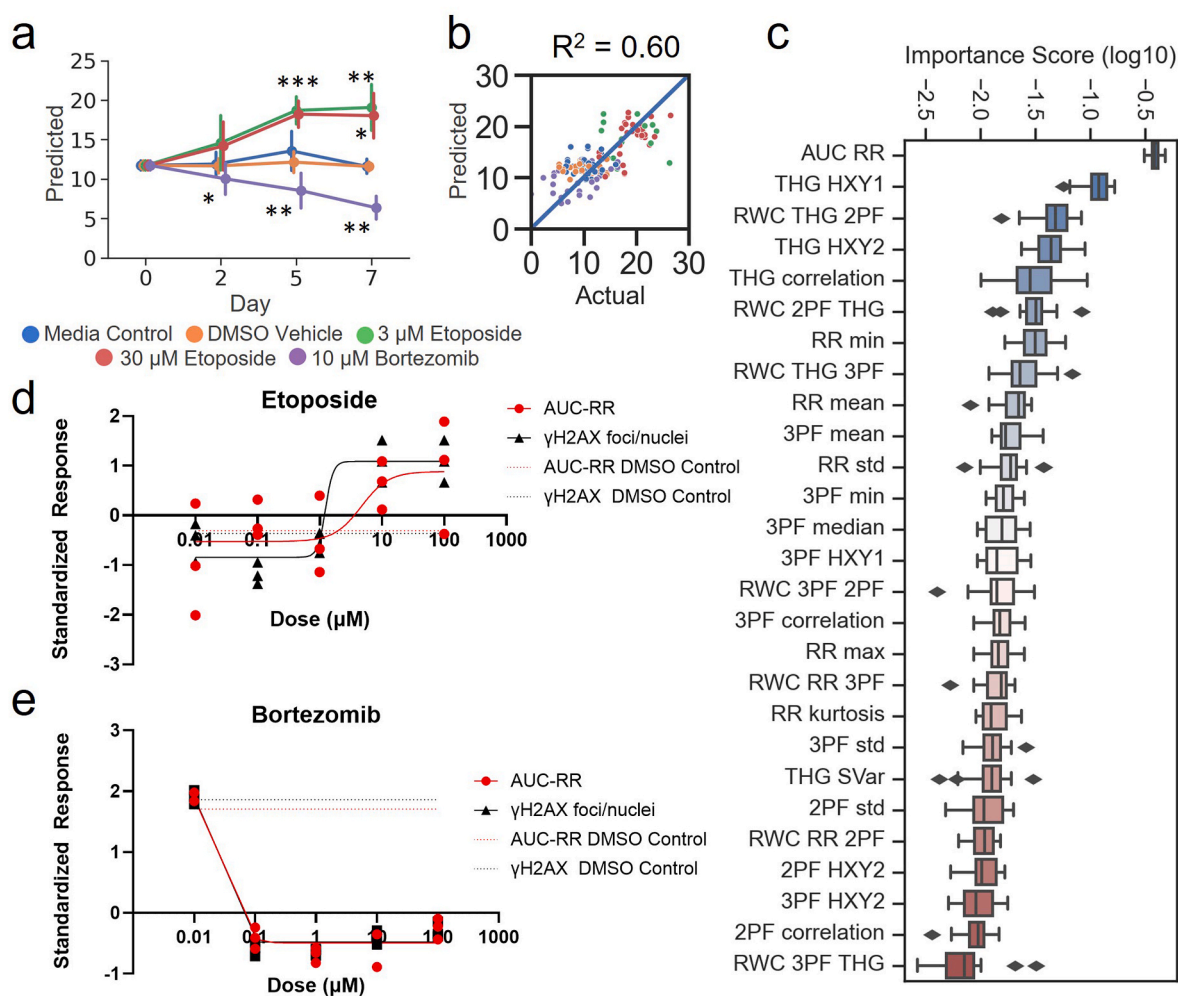
Fig. 4. Performance of the DNA damage prediction model relies on area under the curve of redox ratio (AUC RR). a) Predicted γH2AX foci/nuclei were generated based on 80/20 training/test splits. Statistical testing was performed using ANOVA followed by Tukey's post-hoc test or Kruskal-Wallis followed by Dunn's post-hoc test across all groups within each timepoint. Significance from media control indicated (n = 6–11 replicates, NS = no significance, *p < 0.05, **p < 0.01, ***p < 0.001). b) Evaluation of the model by plotting predictions versus actual results in a R^2 score of 0.60. c) Ranked feature importance scores of SLAM features show relative contributions towards DNA damage prediction. d) Etoposide dose response generated from SLAM based AUC-RR feature and γH2AX foci/nuclei in HUB-047 monolayers at Day 5. SLAM IC50: 4.655 μM, γH2AX IC50: 1.237 μM (3 biological replicates with 3 random fields of view for SLAM imaging and 25 fields of view for γH2AX foci immunofluorescence imaging). e) Bortezomib dose response generated from SLAM based AUC-RR feature and γH2AX foci/nuclei in HUB-047 monolayers at Day 5. SLAM IC50: 0.4511 μM, γH2AX IC50: 0.1245 μM (3 biological replicates with 3 random fields of view for SLAM imaging and 25 fields of view for γH2AX foci immunofluorescence imaging).

identify susceptibility of a sample to treatments causing DNA damage.

4. Discussion

Our objective was to develop a DDR prediction model based on label-free SLAM imaging features for NSCLC organoids to evaluate DNA damaging compounds. The initial hypothesis was that the feature set comprised of label-free intensities, textures, and correlations would suffice in informing DDR prediction. However, this initial hypothesis proved to yield a moderately weak prediction model with a R^2 coefficient of 0.3 (Sfig. 3). Studies examining the link between metabolism and DDR suggest a stronger correlation [12–14], which led to re-examination of the relationship between optical RR, a label-free imaging feature, and cell metabolism. After examining the feature set and how it relates to γH2AX signal, we created a handcrafted feature denoted as AUC-RR to capture a hypothesized relationship between the measured optical RR and DDR (Sfig. 2). This feature makes two key assumptions that differ from before: 1) optical RR is linearly related to the rate of change of cell metabolism, rather than metabolic state itself, 2) the measured optical RR is a combination of a baseline RR and an

effect RR. Derivation of AUC-RR based on those two assumptions can be seen in Supplemental Fig. 2. By incorporating AUC-RR, the model performance increased to 0.6, indicating good DDR prediction based on SLAM imaging features. Moreover, in subsequent experiments with additional DNA damaging compounds and organoid lines, this feature demonstrated trends that were consistent with the initial training experiment (Figs. 3b, 4d and 5e, 6d).

Based on the high feature ranking of AUC-RR compared to the optical RR, the optical RR intensity appears to better indicate the rate of cell metabolism change rather than indicating an absolute measure of metabolic state. We speculate that as cells shift their energy needs as a result of a treatment, upstream pathways which maintain a homeostatic balance of intracellular FAD+ and NAD(P)H are perturbed, resulting in a change in optical RR intensity. After these cells have responded terminally to stimuli, FAD+ and NAD(P)H levels return to baseline levels in the remaining cells, while the outcome of the altered metabolism, γH2AX foci expression or cell death, endures as seen in Fig. 2c and d. While the prediction model does not explicitly show the relationship between AUC-RR and DDR, experimental results suggest that AUC-RR and DDR are increased in tandem (Fig. 2b-d) and in proportion
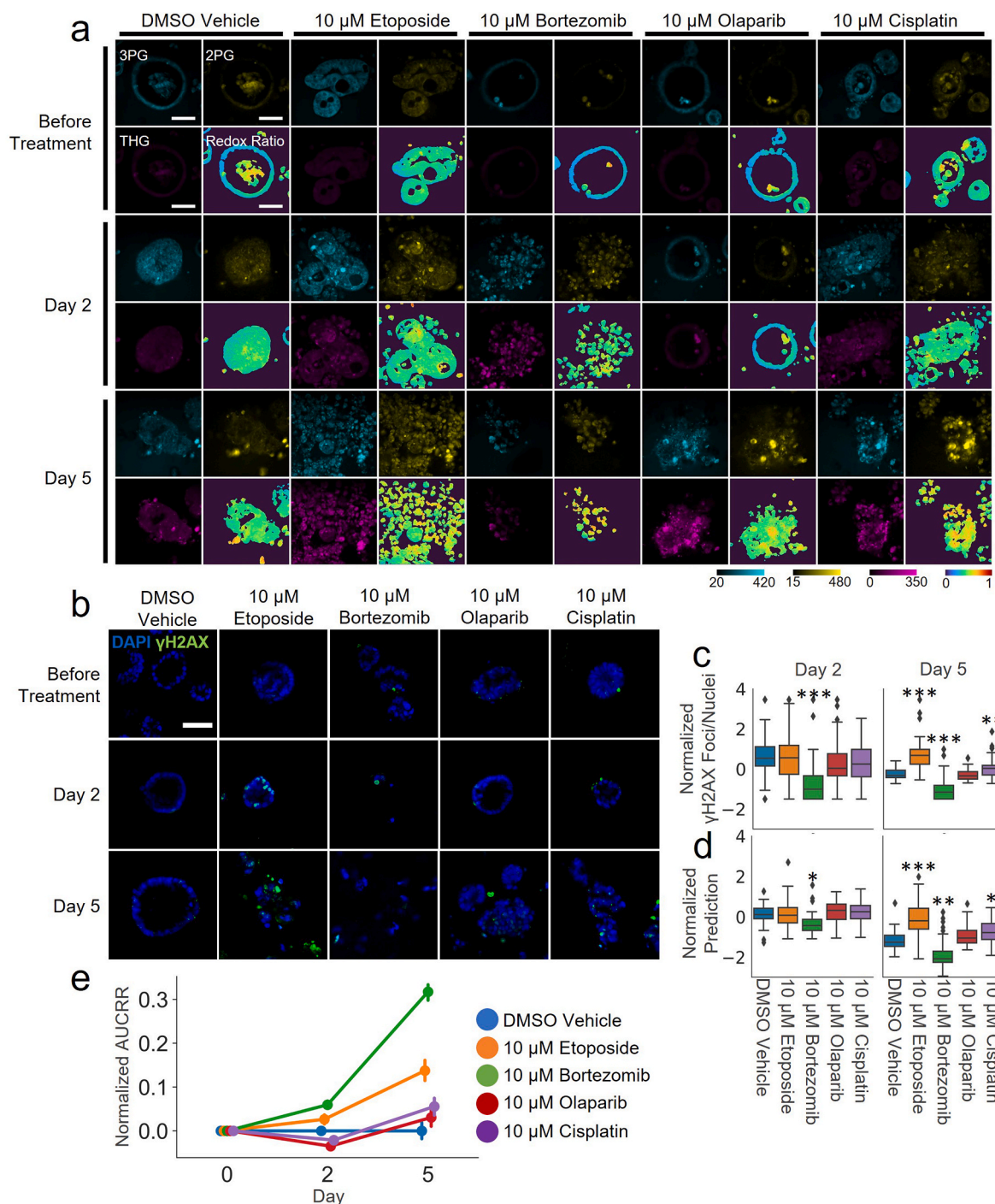
Fig. 5. Implementation of DNA damage prediction model generated from 2D organoids show agreement in 3D organoids. 3D organoids from a treatment naïve patient were cultured in 80 % Matrigel and were continuously treated over 5 days in 10 μm of etoposide, bortezomib, olaparib, or cisplatin. a) Representative 3PF, 2PF, THG, and optical redox ratio SLAM images from before treatment, 2 days and 5 days post-treatment. (scalebar: 50 μm) b) Representative immunofluorescence imaging of DAPI and γH2AX signal in treated organoids (scalebar: 50 μm). c) Normalized ground truth data after 2 and 5 days of treatment (3 biological replicates with 16–25 technical replicates per biological replicate). d) Predicted DNA damage after days 2 and 5 of treatment based on SLAM images show agreement with ground truth data (4 biological replicates with 9 technical replicates per biological replicate). e) AUC-RR quantification from SLAM imaging used to inform predictions in figure d. c,d) Statistical testing was performed using ANOVA followed by Tukey's post-hoc test or Kruskal-Wallis followed by Dunn's post-hoc test across all groups within each timepoint. Dotted boxes were used to denote shared significance from media control (*p < 0.05, **p < 0.01, ***p < 0.001).

(Fig. 5c and e) which aligns with the previous studies demonstrating the metabolic demands of DDR [12–14].

Change in AUC-RR was also observed in bortezomib treated organoids, suggesting that while AUC-RR is important for DDR prediction, deconvolving DDR from cell death mediated by other mechanisms requires other features. This increased involvement of metabolism leading

to cell death is consistent with prior studies [45]. In addition, we have observed that when AUC-RR is calculated by taking sign changes into account, AUC-RR appears to show a negative trend with bortezomib whereas etoposide shows a positive trend (Fig. 4d and e). Feature importance scoring showed that the DDR prediction model also relied on the THG imaging channel (Fig. 4c). THG signal is generated at biological
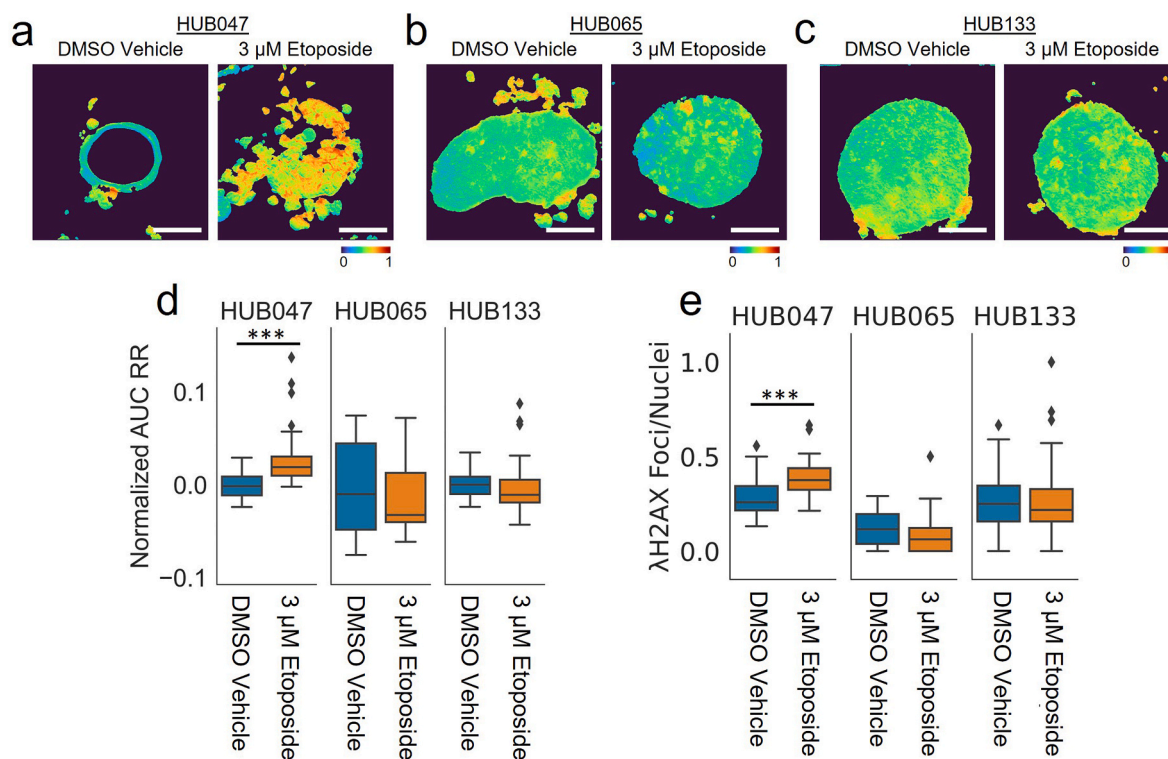
Fig. 6. Lack of response in AUC RR feature suggests resistance to DNA damage. 3D HUB047, HUB065, and HUB133 organoids from 3 different treatment naïve patients were cultured in 80 % Matrigel and were continuously treated with 3 μM etoposide for 3 days. a-c) Representative optical redox ratio image at Day 3 in HUB047, HUB065, and HUB133, respectively (scalebar: 50 μm). d) Normalized AUC RR shows differences at Day 3 in HUB047 line but not in HUB065 or HUB133. (4 biological replicates with 9 technical replicates per biological replicate). e) γH2AX foci/nuclei quantification shows statistical significance only in the HUB047 line, mirroring AUC RR results (3 biological replicates with 10–24 technical replicates per biological replicate). d,e) Statistical testing was performed using ANOVA followed by Tukey's post-hoc test or Kruskal-Wallis followed by Dunn's post-hoc test across all groups within each timepoint. Dotted boxes were used to denote shared significance from media control (*$p < 0.05$, **$p < 0.01$, ***$p < 0.001$).

interfaces where refraction index changes occur, such as at water-lipid and water-protein interfaces [46], and has broad applications in visualizing subcellular structures [35,47,48]. With DNA damage, morphological changes to cellular architecture include extension of the endoplasmic reticulum, dispersal of the Golgi, and mitophagy [49–51]. This reorganization of the cellular architecture may be captured in the THG features, which are sensitive to the spatial organization of interfaces.

A limitation of the label-free approach to DDR predictions is the reliance on time resolved measurements of the optical RR for calculating AUC-RR. Longitudinal SLAM imaging performed at two or three-day intervals provided sufficient time resolution for predictions of DDR in the current study, but for treatments in which cells react over smaller time scales, a high cadence of imaging would be necessary. However, an automated SLAM imaging approach could ensure sufficient time-lapse resolution while allowing for studies to be sufficiently powered. Another limitation is the dependence on the phenotypic response of the specific organoid line, resulting in difficulties translating phenotypic prediction models to other organoid lines. While this study demonstrates that AUC-RR is reflective of treatment sensitivity in organoid lines (Fig. 6), additional validation in cell lines will be necessary to translate these findings more generally. In particular, validation of label-free predictive features towards predicting cisplatin resistance in resistant and XPA deficient cell lines would enable potential use of SLAM based prediction of cisplatin resistance in treating ovarian cancer.

Prediction modeling is an intrinsically data hungry approach. SLAM microscopy, with simultaneous acquisition of four orthogonal, co-registered imaging channels, is tailor-made for generating the longitudinal high-dimensional image datasets needed for prediction modeling. In this study, a SLAM-based DDR prediction model was generated, which

may also be applied non-invasively and non-destructively to tumor organoids with slow growth rates or where deleterious assay optimizations prevent prolonged cell culture. Future studies will examine endpoint predictions beyond DDR to maximize the utility of the rich phenotypic, molecular, and metabolic information captured during SLAM imaging.

5. Conclusion

The goal of this study was to leverage the label-free, non-invasive optical sectioning and imaging capabilities of SLAM microscopy towards the prediction of DDR in live NSCLC organoids. Training and initial testing of the prediction model was successfully performed on 2D NSCLC organoids treated with etoposide, a DNA damaging agent, and bortezomib, a proteasome inhibitor. This prediction model was additionally validated on SLAM imaging of NSCLC organoids in the original 3D format, treated with etoposide, bortezomib, olaparib, or cisplatin. Lastly, imaging and examination of NSCLC organoids with varying susceptibility to etoposide showed that the AUC-RR alone may be a generalizable feature capable of informing DDR across 3D organoid lines. This study demonstrated that non-invasive SLAM-based metabolic imaging via the optical RR and structural imaging with THG was sufficient to predict DDR in live NSCLC organoids. Use of this technique enables rapid phenotypic validation in a physiologically relevant disease model of NSCLC for cancer drugs targeting DNA repair pathways.

Funding sources

Technology on the campus of the University of Illinois at Urbana-Champaign.

CRediT authorship contribution statement

Terrence T. Roh: Writing – review & editing, Writing – original draft, Visualization, Validation, Software, Project administration, Methodology, Investigation, Data curation, Conceptualization. **Aneesh Alex:** Writing – review & editing, Methodology, Conceptualization. **Prasanna M. Chandramouleeswaran:** Writing – review & editing, Methodology. **Janet E. Sorrells:** Writing – review & editing, Methodology, Data curation. **Alexander Ho:** Software. **Rishyashring R. Iyer:** Software. **Darold R. Spillman:** Project administration. **Marina Marjanovic:** Writing – review & editing, Supervision, Project administration, Conceptualization. **Jason E. Ekert:** Writing – review & editing, Supervision, Project administration, Conceptualization. **BanuPriya Sridharan:** Writing – review & editing, Supervision, Project administration, Methodology, Conceptualization. **Balabhaskar Prabhakarpandian:** Writing – review & editing, Supervision, Project administration. **Steve R. Hood:** Writing – review & editing, Supervision, Project administration, Conceptualization. **Stephen A. Boppart:** Writing – review & editing, Supervision, Project administration, Conceptualization.

Declaration of competing interest

The authors declare the following financial interests/personal relationships which may be considered as potential competing interests:
Stephen Boppart is co-founder of and holds equity interest in LiveBx, LLC, which specializes in consulting and building novel multimodal multiphoton imaging systems.

Data availability

Data underlying the results presented in this article are not publicly available at this time, but may be obtained from the authors upon reasonable request and through a collaborative agreement.

Appendix A. Supplementary data

Supplementary data to this article can be found online at https://doi.org/10.1016/j.redox.2024.103280.

References

[1] N.J. O'Neil, M.L. Bailey, P. Hieter, Synthetic lethality and cancer, Nat. Rev. Genet. 18 (10) (2017) 613–623.
[2] R. Nagel, E.A. Semenova, A. Berns, Drugging the addict: non-oncogene addiction as a target for cancer therapy, EMBO Rep. 17 (11) (2016) 1516–1531.
[3] T.T. Paull, et al., A critical role for histone H2AX in recruitment of repair factors to nuclear foci after DNA damage, Curr. Biol. 10 (15) (2000) 886–895.
[4] H. Keles, et al., A scalable 3D high-content imaging protocol for measuring a drug induced DNA damage response using immunofluorescent subnuclear γH2AX spots in patient derived ovarian cancer organoids, ACS Pharmacol. Transl. Sci. 6 (1) (2023) 12–21.
[5] I. Lukonin, M. Zinner, P. Liberali, Organoids in image-based phenotypic chemical screens, Exp. Mol. Med. 53 (10) (2021) 1495–1502.
[6] Y. Yan, et al., Fluorescence intensity and lifetime imaging of lipofuscin-like autofluorescence for label-free predicting clinical drug response in cancer, Redox Biol. 59 (2023) 102578.
[7] A.D. Meade, et al., Prediction of DNA damage and G2 chromosomal radio-sensitivity *ex vivo* in peripheral blood mononuclear cells with label-free Raman micro-spectroscopy, Int. J. Radiat. Biol. 95 (1) (2019) 44–53.
[8] W.R. Zipfel, R.M. Williams, W.W. Webb, Nonlinear magic: multiphoton microscopy in the biosciences, Nat. Biotechnol. 21 (11) (2003) 1369–1377.
[9] B. Chance, et al., Intracellular oxidation-reduction states *in vivo*, Science 137 (3529) (1962) 499–508.
[10] B. Chance, et al., Oxidation-reduction ratio studies of mitochondria in freeze-trapped samples. NADH and flavoprotein fluorescence signals, J. Biol. Chem. 254 (11) (1979) 4764–4771.
[11] K. Alhallak, et al., Optical redox ratio identifies metastatic potential-dependent changes in breast cancer cell metabolism, Biomed. Opt Express 7 (11) (2016) 4364–4374.
[12] A. Moretton, J.I. Loizou, Interplay between cellular metabolism and the DNA damage response in cancer, Cancers 12 (8) (2020) 2051.
[13] M.M. Murata, et al., NAD+ consumption by PARP1 in response to DNA damage triggers metabolic shift critical for damaged cell survival, Mol. Biol. Cell 30 (20) (2019) 2584–2597.
[14] N. Xie, et al., NAD+ metabolism: pathophysiologic mechanisms and therapeutic potential, Signal Transduct. Targeted Ther. 5 (1) (2020) 227.
[15] A.M. Moore, et al., NAD+ depletion by type I interferon signaling sensitizes pancreatic cancer cells to NAMPT inhibition, vol. 118, 2021 e2012469118, 8.
[16] K.P. Quinn, et al., Quantitative metabolic imaging using endogenous fluorescence to detect stem cell differentiation, Sci. Rep. 3 (2013) 3432.
[17] D.A. Gil, D. Deming, M.C. Skala, Patient-derived cancer organoid tracking with wide-field one-photon redox imaging to assess treatment response, J. Biomed. Opt. 26 (3) (2021).
[18] E. Driehuis, et al., Pancreatic cancer organoids recapitulate disease and allow personalized drug screening, Proc. Natl. Acad. Sci. USA 116 (52) (2019) 26580–26590.
[19] H. Tiriac, et al., Organoid profiling identifies common responders to chemotherapy in pancreatic cancer, Cancer Discov. 8 (9) (2018) 1112–1129.
[20] Y. Hu, et al., Lung cancer organoids analyzed on microwell arrays predict drug responses of patients within a week, Nat. Commun. 12 (1) (2021) 2581.
[21] S.-Y. Kim, et al., Modeling clinical responses to targeted therapies by patient-derived organoids of advanced lung adenocarcinoma, Clin. Cancer Res. 27 (15) (2021) 4397–4409.
[22] M.-A. Bray, et al., Cell Painting, a high-content image-based assay for morphological profiling using multiplexed fluorescent dyes, Nat. Protoc. 11 (9) (2016) 1757–1774.
[23] J. Shi, et al., Weakly supervised identification of microscopic human breast cancer-related optical signatures from normal-appearing breast tissue, Biomed. Opt Express 14 (4) (2023) 1339–1354.
[24] S. You, et al., Label-free deep profiling of the tumor microenvironment, Cancer Res. 81 (9) (2021) 2534–2544.
[25] Y. Sun, et al., Real-time three-dimensional histology-like imaging by label-free nonlinear optical microscopy, Quant Imaging Med Surg 10 (11) (2020) 2177–2190.
[26] S. You, et al., Intravital imaging by simultaneous label-free autofluorescence-multiharmonic microscopy, Nat. Commun. 9 (1) (2018) 2125.
[27] J. Park, et al., Label-free optical redox ratio from urinary extracellular vesicles as a screening biomarker for bladder cancer, Am. J. Cancer Res. 12 (5) (2022) 2068–2083.
[28] H. Tu, et al., Stain-free histopathology by programmable supercontinuum pulses, Nat. Photonics 10 (8) (2016) 534–540.
[29] C. Pleguezuelos-Manzano, et al., Establishment and culture of human intestinal organoids derived from adult stem cells, Curr Protoc Immunol 130 (1) (2020) e106.
[30] B. van der Hee, et al., Optimized procedures for generating an enhanced, near physiological 2D culture system from porcine intestinal organoids, Stem Cell Res. 28 (2018) 165–171.
[31] J.H. Lee, et al., Simultaneous label-free autofluorescence and multi-harmonic imaging reveals *in vivo* structural and metabolic changes in murine skin, Biomed. Opt Express 10 (10) (2019) 5431–5444.
[32] D.R. Stirling, et al., CellProfiler 4: improvements in speed, utility and usability, BMC Bioinf. 22 (1) (2021) 433.
[33] S. Berg, et al., ilastik: interactive machine learning for (bio)image analysis, Nat. Methods 16 (12) (2019) 1226–1232.
[34] R.K.P. Benninger, D.W. Piston, Two-photon excitation microscopy for the study of living cells and tissues, Curr. Protoc. Cell Biol. 4 (2013) 4.11.1–4.11.24. Chapter.
[35] S. You, et al., Label-free visualization and characterization of extracellular vesicles in breast cancer, Proc. Natl. Acad. Sci. USA 116 (48) (2019) 24012–24018.
[36] S.M. Sternisha, et al., Longitudinal monitoring of cell metabolism in biopharmaceutical production using label-free fluorescence lifetime imaging microscopy, Biotechnol. J. 16 (7) (2021) e2000629.
[37] O.I. Kolenc, K.P. Quinn, Evaluating cell metabolism through autofluorescence imaging of NAD(P)H and FAD, Antioxid Redox Signal 30 (6) (2019) 875–889.
[38] M.C. Skala, et al., In vivo multiphoton microscopy of NADH and FAD redox states, fluorescence lifetimes, and cellular morphology in precancerous epithelia, Proc. Natl. Acad. Sci. USA 104 (49) (2007) 19494.
[39] T. Mujtaba, Q.P. Dou, Advances in the understanding of mechanisms and therapeutic use of bortezomib, Discov. Med. 12 (67) (2011) 471–480.
[40] A. Montecucco, F. Zanetta, G. Biamonti, Molecular mechanisms of etoposide, EXCLI journal 14 (2015) 95–108.
[41] A. Mehta, J.E. Haber, Sources of DNA double-strand breaks and models of recombinational DNA repair, Cold Spring Harb Perspect Biol 6 (9) (2014) a016428.
[42] M.M. Vilenchik, A.G. Knudson, Endogenous DNA double-strand breaks: production, fidelity of repair, and induction of cancer, Proc Natl Acad Sci U S A 100 (22) (2003) 12871–12876.
[43] R.M. Haralick, K. Shanmugam, I. Dinstein, Textural features for image classification, IEEE Transactions on Systems, Man, and Cybernetics SMC-3 (6) (1973) 610–621.
[44] V.R. Singan, J.C. Simpson, Implementation of the rank-weighted co-localization (RWC) algorithm in multiple image analysis platforms for quantitative analysis of microscopy images, Source Code Biol. Med. 11 (2016) 2.
[45] D.R. Green, L. Galluzzi, G. Kroemer, Metabolic control of cell death, Science 345 (6203) (2014) 1250256.
[46] B. Weigelin, G.-J. Bakker, P. Friedl, Third harmonic generation microscopy of cells and tissue organization, J. Cell Sci. 129 (2) (2016) 245.

[47] M. Rehberg, et al., Label-free 3D visualization of cellular and tissue structures in intact muscle with second and third harmonic generation microscopy, PLoS One 6 (11) (2011) e28237.

[48] C.-H. Wu, et al., Imaging Cytometry of human Leukocytes with third harmonic generation microscopy, Sci. Rep. 6 (1) (2016) 37210.

[49] P. Zheng, et al., DNA damage triggers tubular endoplasmic reticulum extension to promote apoptosis by facilitating ER-mitochondria signaling, Cell Res. 28 (8) (2018) 833–854.

[50] S.E. Farber-Katz, et al., DNA damage triggers Golgi dispersal via DNA-PK and GOLPH3, Cell 156 (3) (2014) 413–427.

[51] J. Kim, et al., Autophagic organelles in DNA damage response, Front. Cell Dev. Biol. 9 (2021).